Synthesis, Characterization, and Application of Gravity-driven Ceramic Microfiltration Membranes for Surface Water Treatment

Yaser Rasouli [a*], Raphaël Maltais-Tariant [b], Benoit Barbeau [a], Mathieu Lapointe [c,d], Caroline Boudoux [b], and Dominique Claveau-Mallet [a]

[a] Department of Civil, Geological & Mining Engineering, Polytechnique Montréal, 2900 Boulevard Édouard-Montpetit, Montréal, Québec, H3T 1J4, Canada

[b] Department of Engineering Physics, Polytechnique Montréal, 2900 Édouard-Montpetit, Montréal, Québec, H3T 1J4, Canada

[c] École de Technologie Supérieure, Université du Québec, 1100 Notre-Dame Ouest, Montréal, Québec, H3C 1K3, Canada

[d] Department of Chemical Engineering, McGill University, Wong Building, 3610 University, Montréal, Québec, H3A 0C5, Canada

[*]Corresponding author. Email: dominique.claveau-mallet@polymtl.ca

Keywords

Biofouling layer, Optical coherence tomography, Drinking water, kaolin, alumina

Abstract

Gravity-driven ceramic microfiltration disk-shaped membranes were synthesized using kaolin and different alumina contents (0% wt, 25% wt, and 50% wt). The pure water flux, mean pore size, porosity and contact angle of membranes were measured. Their structure and composition were characterized by scanning electron microscopy (SEM) and X-ray diffraction (XRD). The effect of alumina content was evaluated for long-term river water filtration in terms of permeate flux, turbidity, dissolved organic carbon (DOC), UV_{254}, pH, and alkalinity removal. The physical characteristics of the biofouling layer, such as thickness and roughness, were studied using optical coherence tomography (OCT) imaging and the concentration of active microorganisms in the biofilm. The results showed acceptable turbidity removal after the flux stabilization period and relatively high performance for DOC, UV, and alkalinity removal during the first three days of filtration. Flux stabilized at 2.5–3 LMH on day 24 of filtration, indicating that the alumina content does not considerably affect the stable flux. As the flux modeling data showed, prior to the flux stabilization time, the fouling was controlled by the pore blocking mechanism. This was confirmed by OCT imaging that showed a very outspread biofilm layer with a low relative roughness; the layer became more compact with a higher relative roughness over time, showing that the cake layer is dominant after the flux stabilization period. Increasing the alumina content of the membranes increased the number of active microorganisms in the biofilm layer; possibly because of an increased adsorption of nutrients in the biofouling layer.

1- Introduction

Although it is of paramount importance for every community to access safe drinking water, achieving this goal can be challenging for small and remote communities that have limited access to trained operators. Providing passive water treatment systems is an appealing option for small systems, as they minimize human intervention and maintenance needs. Consequently, these systems require lower operation and maintenance costs (Shao, Feng et al. 2017) and provide long-term treatment options and minimal supervision (Derlon, Mimoso et al. 2014).

Gravity-driven membrane (GDM) filtration, initially proposed by Peter-Varbanets et al. (2010), is a passive water treatment process that requires a very simple setup and low transmembrane pressure (TMP). A low TMP (normally below 0.1 bar) enables gravity-fed operation and leads to a low stable flux, roughly between 1 and 15 LMH (Pronk, Ding et al. 2019). During long-term filtration, a biofilm grows on the membrane surface, and its presence is considered an important factor in flux stabilization (Truttmann, Su et al. 2020). Numerous studies have demonstrated the possibility of using polymeric membranes in GDM applications, including river water (Peter-Varbanets, Hammes et al. 2010, Klein, Zihlmann et al. 2016, Shao, Feng et al. 2017), pond and tap water (Oka, Khadem et al. 2017), rainwater (Ding, Liang et al. 2017), and seawater (Wu, Suwarno et al. 2017). Among the past investigations, some focused on the relationship between stabilized flux and biofilm (Akhondi, Wu et al. 2015), while others investigated the effect of biofilm on permeate quality (Derlon, Mimoso et al. 2014) and some studied biofilm structure (Derlon, Koch et al. 2013). However, to date, only a limited number of researchers have studied the application of gravity-driven ceramic microfiltration membranes (GDCM) despite the fact that ceramic membranes have high mechanical, chemical, and thermal resistance and a prolonged lifespan (Issaoui and Limousy 2019, Du, Liu et al. 2021). Using kaolin as a starting material decreases the sintering temperature, which in turn decreases the synthesis cost. In some cases, kaolin-based ceramic membranes are more cost-effective compared to polymeric membranes (Hubadillah, Othman et al. 2018). In this regard, Du et al. (2021) studied manganese removal from synthetic water (mixing double-distilled water with $MnSO_4$, $CaCl_2$, $NaHCO_3$, and NaCl) using commercial disk-shaped 300-kDa ZrO_2/TiO_2 membranes (pre-coated with manganese oxides) and 15-kDa ZrO_2/TiO_2 membranes. Their results showed that surface modification (pre-coating with manganese) was beneficial and enabled 75% manganese removal. They also investigated manganese removal following pre-deposition of manganese oxides and powdered activated carbon

on the GDCM surface (Du, Liu et al. 2021). Pre-deposition improved the rejection and concentration of manganese oxidizing bacteria on the membrane surface. There is a scientific gap in the use of cost-effective kaolin-based ceramic membranes for GDM filtration in drinking water applications.

The general objective of this study was to investigate the feasibility of using affordable kaolin-based ceramic membranes operated in a gravity-driven mode to filter colored surface water. The sub-objectives were to 1) investigate the effect of alumina concentration in the membrane structure on the flux, permeate quality, and biofilm layer properties and 2) study the fouling mechanisms of the membranes by flux-decline data modeling and biofilm characterization. To achieve these objectives, disk-shaped ceramic microfiltration (MF) membranes composed of kaolin and alumina were synthesized using pressure casting and sintering. Virgin and colonized membranes were characterized, and their performances in treating surface water were assessed and compared. Biofilm development was studied using OCT and adenosine triphosphate (ATP) methods.

2- Materials and Methods

2.1. Membrane synthesis

Ceramic MF membranes were synthesized using the pressure casting and sintering method (Hubadillah, Othman et al. 2018). Pure kaolin clay (Sheffield Pottery, Sheffield, MA, USA, Table 1), alumina powder (Fisher Scientific, Switzerland; Al_2O_3, 40–300 μm, CAS: 1344-28-1, Mw = 101.96 g mol^{-1}), boric acid (Ward's Science, Rochester, NY, USA; H_3BO_3, CAS: 10043-35-3, crystals), and deionized (DI) water were used as the starting materials for membrane synthesis.

Table 1. Composition of kaolin used to synthesize membranes

Compounds	Value (%)	Compounds	Value (%)
SiO_2	45.73	CaO	0.18
Al_2O_3	37.36	MgO	0.01
Fe_2O_3	0.79	Na_2O	0.06
TiO_2	0.37	K_2O	0.33
P_2O_5	0.24	Loss on ignition (LOI)	13.91

To make a suitable dough for molding, DI water was gradually added to the kaolin and alumina powder, and then boric acid was added at 10% by wt of kaolin. Boric acid was used to increase

the mechanical strength of the membrane. The mixture was mixed for 10 minutes using a high-power mechanical mixer at 100 rpm (Masterflex L/S® Analog Variable-Speed Modular Drive, Cole-Parmer Instrument Co., Canada) with four blades to obtain a uniform dough. The dough was transferred to a disk-shaped mold, and pressure was applied using a clamp. Each disk-shaped membrane had a diameter, thickness, and area of 43 mm, 5 mm, and 14 cm^2, respectively. The membranes were kept at 22-25 ˚C for at least 24 hours to dry. The dried membranes were sintered in a programmable electrical furnace (Ney Vulcan, 3-550). Table 2 summarizes the calcination steps. After calcination, the membranes remained in the furnace for at least 8 hours to avoid sudden changes in the temperature leading to membrane breakage. The ratios of the kaolin/alumina used in membranes M1, M2, and M3 are listed in Table 3. Three membranes of each type (M1, M2, and M3) were synthesized for the filtration experiments and membrane characterization.

Table 2. Membrane sintering procedure

Temperature range	Temperature ramp
25 °C –550 °C	3 °C/min
550 °C	0 (for 2 hours)
550 °C–750 °C	3 °C/min
750 °C	0 (for 2 hours)
750 °C–1100 °C	2 °C/min
1100 °C	0 (for 2 hours)

Table 3. Composition of different types of synthesized membrane

Membrane type	Wt% kaolin	Wt% alumina
M1	100	0
M2	75	25
M3	50	50

2.2. Influent water source

Influent water was collected in August 2021 from the Pont-Viau drinking water treatment plant (Laval, Canada), which is fed by the des Prairies River. The influent stock barrel was maintained at 4 °C. To ensure a constant temperature in the system, 20 L of the influent water was collected

from the stock barrel every week and incubated at room temperature for 5 hours prior to use. The influent water characteristics are listed in Table 4.

Table 4. Influent water characterization

Parameters	Mean value	Max value	Min value	Standard deviation	Number of samples
DOC (mg L^{-1})	6.51	7.76	5.82	0.43	22
Turbidity (NTU)	2.30	2.45	2.05	0.13	21
pH	7.58	7.68	7.49	0.06	21
Alkalinity (mg $CaCO_3$ L^{-1})	18	22	12	4.80	21
UV_{254} (cm^{-1})	0.18	0.22	0.16	0.01	21

2.3. Gravity-driven filtration experiments

Three membrane modules were fed in parallel with influent water for 65 days, as shown in Figure 1 and Figure S1. A constant head of 90 mbar (~90 cm H_2O) was maintained by continuously pumping influent water from the influent water tank into the overhead tank with a permanent overflow. Permeates were collected daily for quality measurements and flux calculations. The temperature was monitored using a thermometer placed in the overhead tank and controlled by a laboratory air conditioning system. The mean temperature was 22 °C during the experiment (minimum 21 °C and maximum 24 °C). To avoid algae growth in the system, the entire setup (such as tanks, pipes, permeate containers) was covered by a layer of dark tape and a layer of aluminum foil. Makeup influent water was added to the influent water tank weekly.

The membrane modules were made from polyethylene with a sight glass to allow for visual tracking of cake layer growth and obtain OCT images without removing the membranes from their cells. During OCT imaging, the filtration cells were removed from the system for approximately an hour (without removing the membranes) and replaced after imaging. The permeate weight was measured daily using a digital balance (Sartorius, LC1201S, Germany).

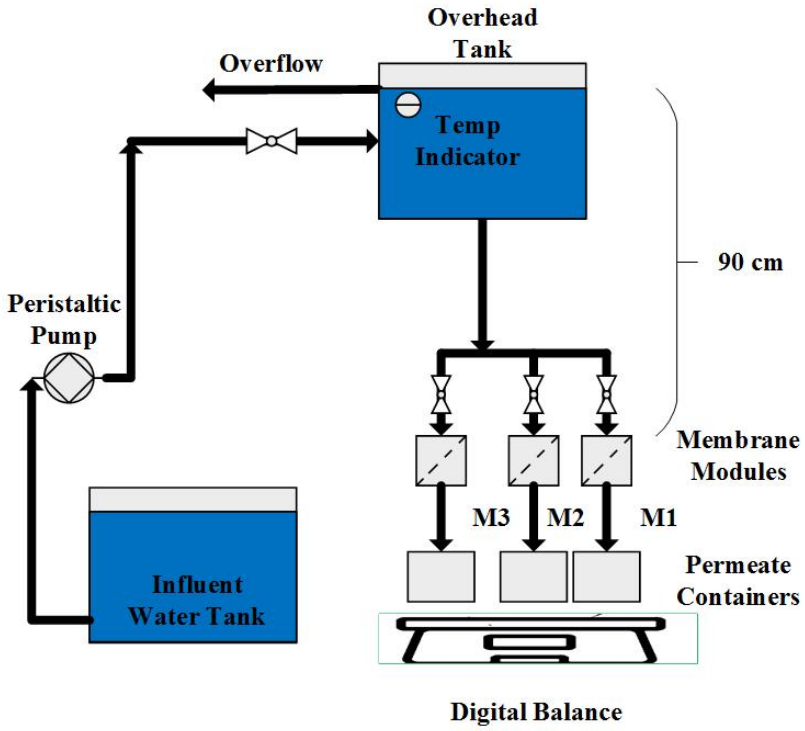

Figure 1. Schematic representation of the experimental setup

2.4. Permeate quality characterization

The influent and permeate were sampled daily for the first week of filtration and then twice a week for the remaining testing period. The collected permeate samples were measured for DOC, turbidity, UV_{254} index, alkalinity, and pH. The samples that could not be analyzed immediately were stored at 4 °C. A DOC analysis was performed on samples filtered with prewashed (1 L) membranes (PES, 0.45-µm, 47 mm, Pall Corporation, Washington, NY, USA) using an online TOC analyzer (Sievers M5310 C, Trevose, PA, USA). UVA_{254} was measured in a 1-cm quartz cell using a UV-visible spectrophotometer (Cary 100 Scan, Varian Inc.). A turbidity meter (TL2300, Hach, USA) was used to measure the turbidity. Before each use, the device was calibrated using standard samples. A pH meter (Accumet AB 15 basic, Fisher Scientific, Waltham, MA, USA) was used to measure the pH. Before each use, the electrode was carefully washed with demineralized water and calibrated using standard solutions (pH = 4, 7, 11). For the alkalinity measurement, 50 ml of the sample was titrated using a 0.02 N H_2SO_4 solution to obtain a pH of 4.5 and then 4.2; alkalinity was calculated using Equation 1.

$$Alkalinity\ (\frac{mg}{l}\ CaCO_3) = \frac{(2B-C)\times 0.02\times 50{,}000}{V}, \text{ Eq. (1)}$$

where B is the consumed volume of H_2SO_4 to reach a pH of 4.5, C is the total volume of H_2SO_4 consumed to reach a pH of 4.2, and V is the volume of the sample.

2.5. Membrane characterization

2.5.1. Pure water flux

Before the start of the filtration experiment, demineralized water was used to obtain the pure water flux expressed in LMH at a mean temperature of 22 °C at 90 mbar. The fluxes were normalized to 20 °C.

2.5.2. Contact angle

The membrane surface was first cleaned with ethanol and dried with Kimwipes™ and pressurized air. The contact angle was measured with a droplet of water using a goniometer (OCA20, Dataphysiscs, Germany) equipped with a video camera. Based on the recorded videos (not shown), the membranes were categorized as highly hydrophilic, with contact angles lower than 5°.

2.5.3. Membrane structure characterization using scanning electron microscopy

Approximately one-quarter of the clean membranes were carefully cut and subjected to SEM analyses. The samples were prepared by vacuum coating with a very thin layer of gold (~60 nm, because the membrane materials are not electron conductive, Polaron SC502 sputter coater) at a pressure of approximately 10 bar and current of 10 mA. The samples were observed on a device (Jeol, JSM-7600TFE, JEOL Ltd., Japan) using low electron voltages (5–10 kV).

2.5.4. Crystalline phase characterization by X-ray diffraction

The clean membranes were crushed to obtain fine powders suitable for XRD analysis using a Brucker D8 Advanced device. The XRD patterns were obtained using Cu-Kα radiation at a rate of 0.2° per step and a time frame of one second per step.

2.5.5. Membrane porosity

Membrane porosity was calculated based on the water mass adsorbed in the membrane structure after immersion in a water bath. The dry membranes were initially weighed (W_1), and then soaked for 72 hours in pure water at a fixed ambient temperature. After soaking, the outer surface dried

using Kimwipes™ and weighed again (W_2). The membrane porosity was calculated as follows (Arzani, Mahdavi et al. 2016):

$$Porosity = \left(\frac{W_1 - W_2}{\rho_m V_m}\right), \text{ Eq. (2)}$$

where ρ_m and V_m are the density of pure water at the corresponding temperature and membrane volume, respectively.

2.5.6. Membrane mean pore size

The membrane mean pore radius (R_m) was calculated using the Guerout-Elford-Ferry equation (Zhang, Lang et al. 2015) (Equation 3), where ε is the membrane porosity, L is the membrane thickness, μ is the water viscosity at the filtration temperature, J is the membrane flux, and ΔP is the pressure.

$$R_m = \sqrt{\frac{(2.9 - 1.75\,\epsilon) 8\mu\, L\, J}{\varepsilon\, \Delta P}}\,, \text{ Eq. (3)}$$

2.6. Biofilm characterization

2.6.1. Biofilm growth characterization by OCT

The OCT device used for characterization was the same as that used by the previously published study (Maltais-Tariant, Boudoux et al. 2020). Briefly, a commercial 1310-nm OCT was operated with a balanced detector imaging module. The raw OCT images were processed, then analyzed using ImageJ software (NIH, USA) to obtain the relative thickness of the biofilm layer. The thickness was measured by determining manually the position of the membrane surface over 4 scans taken over 10.9 mm on different areas of the membranes. The pixel thickness was then converted in optical thickness (Z_f) using the µm/pixel ratio. Since OCT measures optical distance axially, the physical thickness (Z_i) was calculated using Equation 4 (Fujimoto and Drexler 2015) as follows:

$$Z_i = \frac{Z_f}{n_f}, \text{ Eq. (4)}$$

where n_f is the biofilm refractive index. Because of the high water content of the biofilm, its refractive index can be assumed to be equal to that of water (n_f = 1.333) (Bakke, Kommedal et al.

2001). The mean biofilm layer thickness ($\overline{Z}$ in μm), absolute roughness coefficient (Ra in μm), and relative roughness coefficient ($\overline{R}$a) were calculated according to Equations 5 to 7, respectively (Derlon, Peter-Varbanets et al. 2012, Akhondi, Wu et al. 2015). In this study, the thickness was calculated using OCT images only at the end of the filtration time (on the day 65).

$$\overline{Z} = \frac{1}{n}\sum_{i=1}^{n} Z_i \quad \text{Eq. (5)}$$

$$R_a = \frac{1}{n}\sum_{i=1}^{n}\left(\left|Z_i - \overline{Z}\right|\right) \quad \text{Eq. (6)}$$

$$\overline{R}_a = \frac{1}{n}\sum_{i=1}^{n}\left(\frac{\left|Z_i - \overline{Z}\right|}{\overline{Z}}\right) \quad \text{Eq. (7)}$$

Here, n is the number of calculated thicknesses, and Z_i (in μm) is the biofilm thickness at each point.

2.6.2. Biofilm activity characterization using ATP method

Briefly, approximately one-eighth of the membranes after the filtration experiment were carefully cut and placed in 50 ml of sterile phosphate buffer saline, which was sonicated for 2 minutes at 40 W power and 20 KHz (Cole-Parmer Ultrasonic processor, Canada). This procedure was repeated six times, each time with fresh 50 mL sterile phosphate buffer. Thereafter, 30 mL of composite sample was produced by mixing equivalent volumes from each sonicated sub-sample. To measure the extracellular ATP, the composite sample was filtered through a syringe filter (0.2-μm, Quench-Gone, DIS-SFQG-25, LuminUltra, USA) to retain any microorganisms on the filter, and then lysed using Ultralyse 7 solution (LuminUltra, USA) to recover the intracellular ATP of the biofilm. Next, a TriStar2 Multimode Reader LB 942 (BERTHOLD Technologies) was used to read the luminescence in RLU/s units after washing the microplate reader with six cycles of ultrapure water and six cycles of luminase. Finally, using a developed calibration curve (0, 10, 25, 100, 250, 500, and 1000 pg/ml, R^2 = 0.9999) by dilution with Ultracheck solution (1000 pg/ml, LuminUltra, USA), the ATP values were reported as a standard ratio of ATP weight (pg)/sample weight (Pg).

2.7. Quartz crystal microbalance with dissipation

The affinities between the natural organic matter (NOM) and membrane-like surfaces were evaluated using a quartz crystal microbalance with dissipation monitoring (QCM-D) (QSense Explorer). The NOM deposition rates were measured on silica (SiO_2; QSense) and alumina sensors

(Al_2O_3; QSense). The Sauerbrey equation (Sauerbrey 1959) can be used to describe the relationship between the deposited mass (in ng/cm^2) and the variation in the resonance frequency of the material (SiO_2 or Al_2O_3 sensor for this study):

$$\Delta m = -\frac{C_{QCM}}{n}\Delta f, \text{ Eq. (8)}$$

where Δm is the change in the mass deposited on the sensor, C_{QCM} is the mass sensitivity constant (e.g., 17.7 ng cm^{-2} Hz $^{-1}$ for a 5 MHz quartz crystal), *n* is the overtone number (1, 3, 5, 7, and 9), and Δf (Hz) is the shift in resonance frequency at overtone *n* (Akanbi, Hernandez et al. 2018).

Before each QCM-D experiment, the SiO_2 and Al_2O_3 sensors were cleaned by soaking them in 2% Hellmanex. The sensors were then bath sonicated for 20 minutes, rinsed 10 times with DI water, rinsed three times with ethanol, rinsed again 10 times with DI water, and dried with nitrogen gas. The sensors were UV-exposed for 2 hours (UV chamber, Bioforce Nanosciences) to remove residual contaminants. DI water and all solutions used during the washing procedure were pre-filtered (0.1-µm cellulose acetate membrane, Corning® 500 mL) to avoid (nano)particles and undesired negative frequency shifts associated with contamination. The experiments were conducted at room temperature, and a peristaltic pump was used to enable operation under laminar flow conditions, while avoiding air bubbles (flow rate of 100 µL/min). Before entering the QCM-D module, the NOM was pre-filtered with a 0.45-µm membrane to avoid larger colloids and erratic deposition rates (Lapointe, Farner et al. 2020).

2.8. Flux calculation and fouling resistance modeling

The flux was calculated by dividing the daily volume of the permeate by the membrane area. The total fouling resistance of the membranes (m^{-1}, R) was obtained using Darcy's law: $R_{total} = \Delta P / (\mu_T J_T)$, where μ_T is the permeate viscosity at temperature T, J_T is the measured permeate flux at temperature T, and ΔP is the hydrostatic pressure. The clean membrane resistance (R_{clean}) was calculated using the same procedure as that used for the pure water flux. The fouling resistance (biofilm and irreversible resistance) was calculated by subtracting the clean membrane resistance (R_{clean}) from the total fouling resistance (R_{total}).

Hermia's model was used to identify the membrane fouling mechanism during filtration (Hermia 1982). The model can be described by Equation 9, where t is the time of filtration, V is the collected permeate volume, and K is a proportionality constant.

$$\frac{d^2t}{dv^2} = K(\frac{dt}{dv})^n \quad \text{Eq. (9)}$$

In this equation, n depends on the fouling type, as listed in Table S1. A schematic representation of these mechanisms is shown in Figure S2.

3. Results

3.1. Effect of alumina content on membrane properties

The mean porosities of membranes M1, M2, and M3 are listed in Table 5. The mean porosities of M1 and M2 were calculated to be approximately 42% and 44%, respectively, and the difference between them was not significant ($p = 0.11$). However, a significant ($p = 0.02$) increase in porosity (~12%) was observed after increasing the alumina content to 50% in M3. Because alumina is integrated in the membrane structure between kaolin particles, it increases the porosity, pore size, and flux, as shown previously (Rasouli, Abbasi et al. 2017).

Table 5. Results of membrane characterization

Membrane type	M1	M2	M3
Contact angle	<5°	<5°	<5°
Porosity (%)	41.9 ± 0.99	43.6 ± 1.88	54.7 ± 2.1
Mean pore radius (μm) (calculated)	0.43 ± 0.01	0.48 ± 0.01	0.98 ± 0.03
Mean pore radius (μm) (from SEM)	0.37 ± 0.24	0.58 ± 0.23	0.98 ± 0.35
Pure water permeability (LMH/bar) at 90 mbar	101 ± 3	375 ± 18	3851 ± 35
Major phase*	Boromullite	Aluminum borate	Aluminum borate
Minor phase*	SiO_2	SiO_2	SiO_2

*From the XRD analysis.

All membranes were highly hydrophilic, as indicated by their low contact angles (Table 5). The mean pore sizes of M1 and M2 ranged 0.43–0.48 μm and were not statistically different ($p = 0.05$). M3, with the highest alumina content, had a significantly higher mean pore size of 0.98 μm ($p = 0.001$). The XRD patterns of the membranes are illustrated in Figure S3. For M1, the major phase was $Al_9BSi_2O_{19}$ (boromullite), whereas the minor phase detected was SiO_2. For M2 and M3, the phases were identified as aluminum borate and SiO_2, respectively. During the calcination process

at 550 °C, kaolin clay was transformed into metakaolin by dihydroxylation, which is the anhydrous form of kaolin, according to Equation 10.

$$2\ Al_2Si_2O_5(OH)_4 \rightarrow 2\ Al_2Si_2O_7 + 4\ H_2O \quad \text{Eq. (10)}$$

Increasing the temperature to 1050 °C leads to the formation of a mullite phase according to Equation 11 (Rasouli, Abbasi et al. 2019).

$$3\ (Al_2O_3.\ 2SiO_2) \rightarrow 3\ Al_2O_3.\ 2\ SiO_2 + 4\ Si \quad \text{Eq. (11)}$$

Mullite can react with boric acid (which is added to increase the mechanical strength of the membrane) to form a boromullite phase, according to Equations 12 and 13 (Hernández, Violini et al. 2020). The presence of a boromullite phase after membrane calcination indicates the formation of a mullite phase during membrane calcination, which is the major phase in kaolin-based membranes (Rashad, Logesh et al. 2021), indirectly confirming the correct calcination procedure.

$$H_3BO_3 \rightarrow B_2O_3 + H_2O \text{ (boric acid decomposition)} \quad \text{Eq. (12)}$$

$$3\ Al_2O_3.\ 2SiO_2 + B_2O_3 \rightarrow Al_4.5SiB_{0.5}O_{9.5} \text{ (boromullite)} \quad \text{Eq. (13)}$$

The surface micrographs of the membranes are shown in Figure 2. A rough and porous structure was observed for the M3 membrane, confirming the porosity calculated using the wet and dry membrane weights. The porosity results showed that the M3 had the highest porosity. Moreover, as the red circles in the micrograph indicate, the approximate pore sizes were 1 μm, which confirms the calculated mean pore sizes. A smoother, porous, and more compact structure was observed for M2. The SEM observations of the M2 samples showed a mean pore size lower than that of the M3 membrane. The general pattern and structure of the membrane were roughly the same as those of M1, although they were less porous and had a smaller pore size than the M3 membrane.

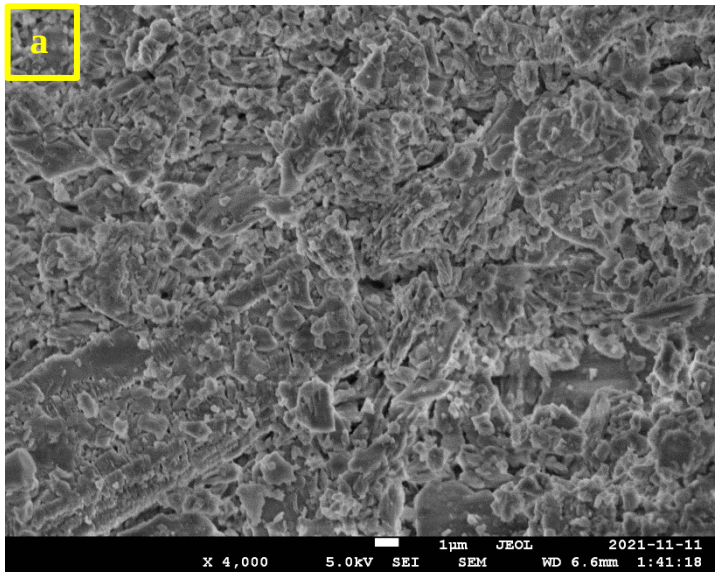
a
1µm JEOL 2021-11-11
X 4,000 5.0kV SEI SEM WD 6.6mm 1:41:18

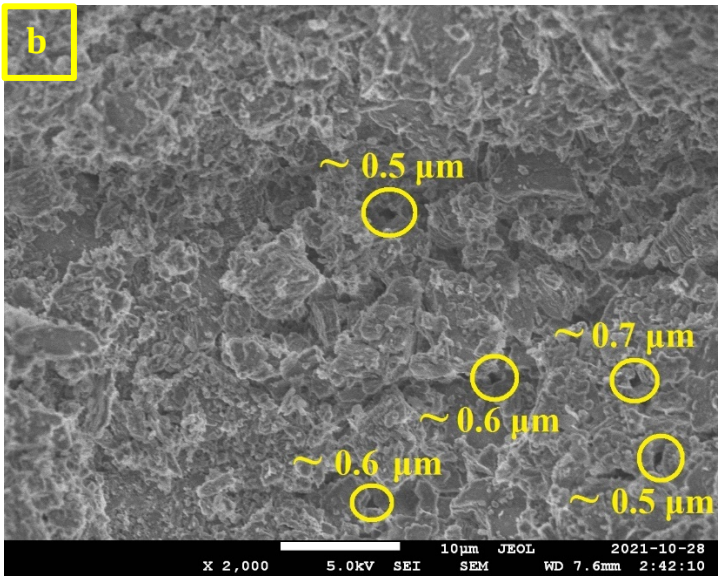
b
~ 0.5 µm
~ 0.7 µm
~ 0.6 µm
~ 0.6 µm
~ 0.5 µm
10µm JEOL 2021-10-28
X 2,000 5.0kV SEI SEM WD 7.6mm 2:42:10

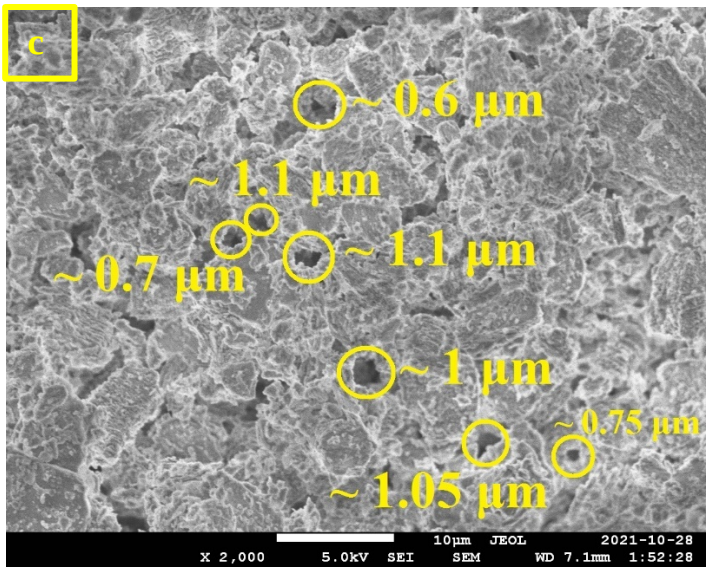

Figure 2. SEM images from the surface of M1 (kaolin only), M2 (75 Wt% kaolin + 25 Wt% alumina), and M3 (50 Wt% kaolin + 50 Wt% alumina) membranes.

At an operating pressure of 90 mbar, the lowest permeability of the pure water was roughly 100 LMH/bar for M1, which then roughly quadrupled for M2 (375 LMH/bar); for the M3, it increased more than 10 times to reach a peak of approximately 3850 LMH/bar, as expected from the results of porosity and mean pore sizes.

3.2. Effect of alumina content on membrane sorption affinity

The results of the NOM deposition in the QCM analysis are presented in Figure 3. The SiO_2 sensor mimics the kaolin-based membrane M1 with high Si content, whereas the Al_2O_3 sensor represents the kaolin plus alumina-based membranes M2 and M3. The frequency shift, representing the NOM deposition on the sensor, is low for SiO_2, which confirms that the soluble NOM molecules in the influent water have low surface interaction with the SiO_2 surface. The NOM deposition rate on the Al_2O_3 sensor was higher than that on the SiO_2 sensor, indicating that the NOM had a higher affinity toward Al-based oxides than Si-based oxides.

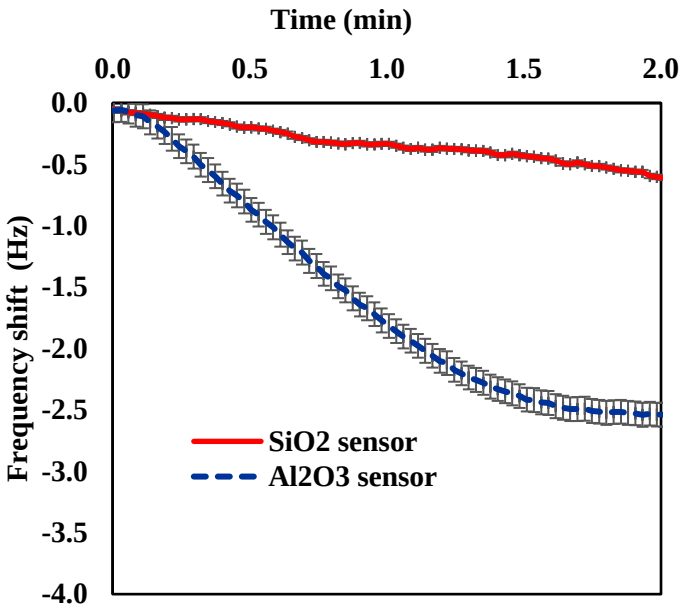

Figure 3. Frequency shift as an indicator of NOM deposition rates on SiO_2 and Al_2O_3 sensors mimicking kaolin-based membrane (M1, red curve) and kaolin+alumina-based membrane (M2 and M3, blue curve), respectively.

3.3. Permeate flux and fouling resistance

The flux decline rates for the tested membranes are shown in Figure 4a (or Figure S4 for improved resolution). The figure can be divided into four phases. The first phase is characterized by a steep flux decrease related to rapid membrane pore blocking. During this phase, the permeate flux dropped from 45 to approximately 2.5 LMH, 17 to 2.2 LMH, and 7 to 2.1 LMH for M3, M2, and M1, respectively. During the second phase, a stable flux was reached after 24 days of filtration for all the membranes.

During the third phase, a slight increase in flux was observed before a stable flux was reached again in the fourth phase, which can be attributed to biofilm growth on the membrane surface that has been shown to improve membrane flux (Du, Liu et al. 2021). The stable fluxes of M1, M2, and M3 were approximately 2.4, 2.5, and 3.0 LMH, respectively.

The same trend was observed for fouling resistance (Figure 4b). For the synthesized M1, M2, and M3 membranes, it first increased sharply to reach a peak of approximately 1.5×10^{10} m^{-1} and then decreased to achieve a stable value of approximately 1.3×10^{10} m^{-1}.

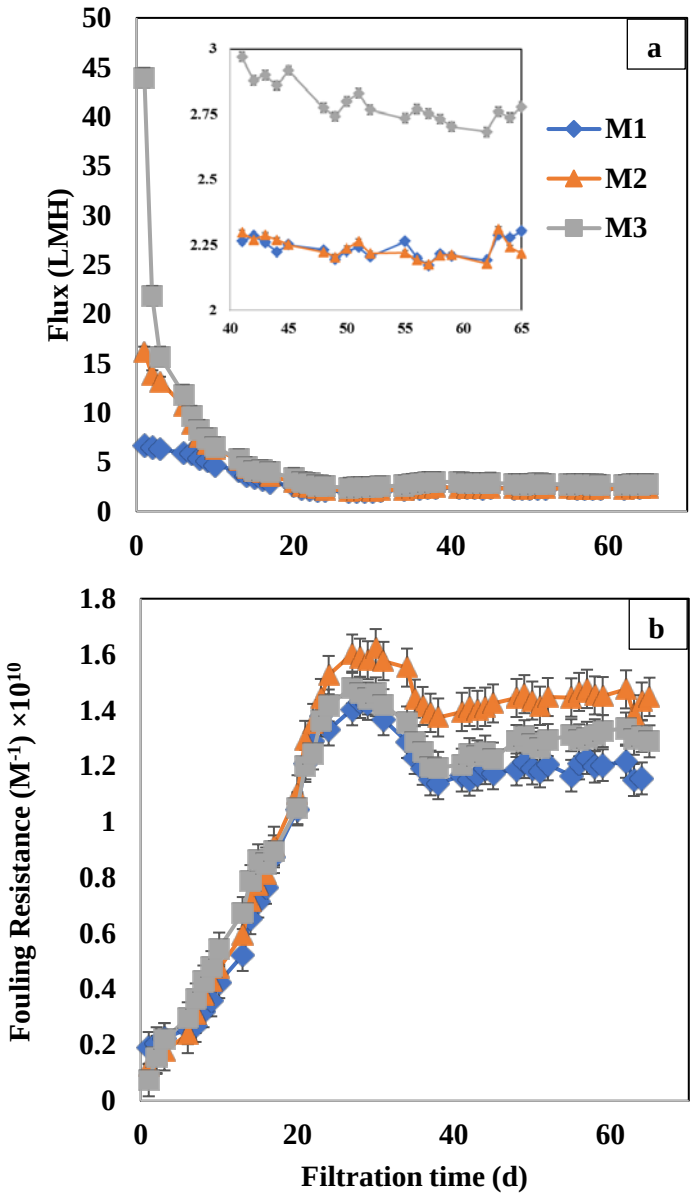

Figure 4. Evolution of a) permeate flux and b) fouling resistance for M1 (kaolin only), M2 (75 Wt% kaolin + 25 Wt% alumina), and M3 (50 Wt% kaolin + 50 Wt% alumina) membranes.

3.4. Membrane fouling mechanisms

The modeling of the flux-time data using pore blocking and cake layer formation mechanisms before reaching the stable flux time are shown in Figure 5, and the percentages of errors between the experimental and modeled fluxes are listed in Table S2. For M1, the standard and complete pore blocking models showed the minimum error between the experimental and modeled data, as

approximately 18% and 15%, respectively. Likewise, for M2, the complete pore blocking model showed the best fit with an error of approximately 14%. For M3, the intermediate pore blocking model with an error of 5% was the best model. Furthermore, the error between the cake layer formation model and experimental data decreased with time. This suggests that in the initial days of filtration, before a stable flux was reached, the internal area of the membrane pores was clogged, and a biofilm layer started to form on the membrane surface toward the flux stabilization time.

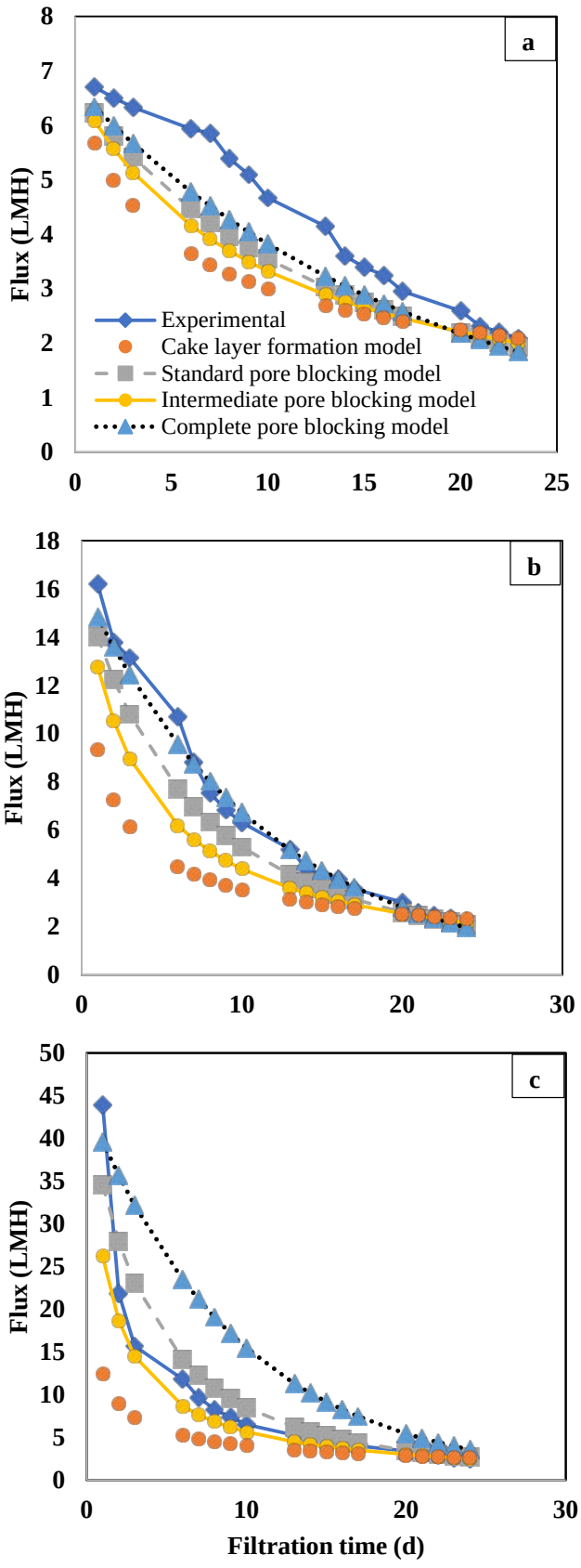
a
b
c
Flux (LMH)
Filtration time (d)
Experimental
Cake layer formation model
Standard pore blocking model
Intermediate pore blocking model
Complete pore blocking model

Figure 5. Flux decline modeling for M1 (kaolin only), M2 (75 Wt% kaolin + 25 Wt% alumina), and M3 (50 Wt% kaolin + 50 Wt% alumina) membranes

3.5. Permeate quality

Permeate turbidity as a function of time is shown in Figure 6a. The highest variations were observed during the first 14 days of filtration. After the first day of filtration, M1 showed a turbidity of approximately 0.9 NTU, which dropped continuously to reach a minimum of approximately 0.2 NTU, followed by a fluctuating trend ranging between 0.2 and 0.3 NTU. Likewise, for M2, the general trend was the same; it started at approximately 0.45 NTU and decreased to approximately 0.1 NTU, finally reaching a stable value of 0.15 NTU. For M3, the turbidity was initially approximately 0.3 NTU, which decreased to around 0.15 NTU and then stabilized at 0.2 NTU. According to the United States Environmental Protection Agency (USEPA), the turbidity of the permeate should be lower than 0.15 NTU. This result suggests that it would be desirable for future assays to use membranes with lower porosities to improve turbidity rejection results.

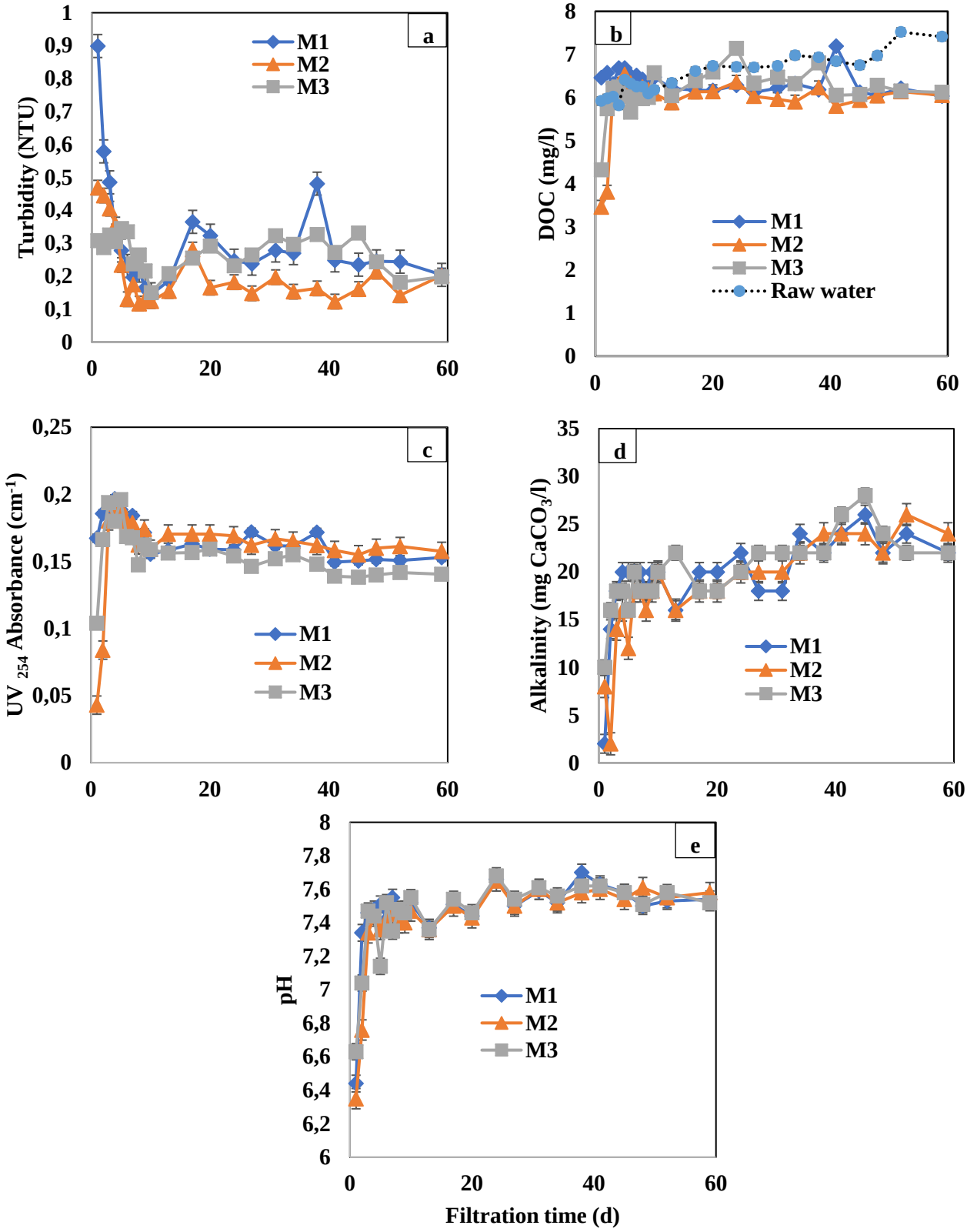
a
Turbidity (NTU)
M1
M2
M3
b
DOC (mg/l)
M1
M2
M3
Raw water
c
UV 254 Absorbance (cm-1)
M1
M2
M3
d
Alkalinity (mg CaCO3/l)
M1
M2
M3
e
pH
M1
M2
M3
Filtration time (d)

Figure 6. Permeate quality variations by time using the three membrane types: M1 (kaolin only), M2 (75 Wt% kaolin + 25 Wt% alumina), and M3 (50 Wt% kaolin + 50 Wt% alumina)
a) Turbidity (NTU), b) DOC (mg/l), c) UV254 index, d) alkalinity (mg/l CaCO3), and e) pH

Figure 6b shows the evolution of DOC in the three permeates and the influent water. At the initial filtration time, the permeates of M2 and M3 showed a lower DOC content of approximately 3.4 and 4.5 mg C/L, respectively, compared to the influent water (~6 mg C/L). However, the NOM removal reached a stable value, fluctuating around 6 mg C/L after one week of operation, which was slightly lower than the DOC influent water.

For M1, a different trend was observed. In the initial filtration time, the initial DOC was 6.5 mg C/L, followed by a slight decrease and finally fluctuating to around 6 mg C/L (similar to M2 and M3 membranes).

The UV_{254} absorbance versus time is plotted in Figure 6c. The general scheme was similar to that of the DOC evolution. Initially, M2 and M3 exhibited significant UV_{254} removal, reaching a minimum value of 0.05 and 0.1, respectively. However, after rapid exhaustion of the alumina adsorption capacity, there was a steep increase in the UV_{254} trend, and a stable state with 0.16 and 0.14 absorbance units was achieved for M2 and M3 permeates, respectively. For the M1, the initial UVA_{254} of the permeate was 0.17 cm^{-1}, followed by a slight increase up to 0.19 cm^{-1} and then a decrease to reach a stable value of approximately 0.14 cm^{-1}.

The evolution of alkalinity and pH is presented in Figure 6d and 6e, respectively. The trends followed a pattern similar to those of DOC and UV_{254}. The M1, M2, and M3 membranes showed a decrease in alkalinity from approximately 20 mg/L $CaCO_3$ (influent water) to 2 mg/L$CaCO_3$, 2 mg/L $CaCO_3$, and 10 mg/L $CaCO_3$, respectively. This may be because acidic moieties present in fresh membrane pores transform bicarbonate ions (HCO_3^-) into H_2CO_3 and eventually CO_2, as the pH of the influent water is always 7.4–7.6; therefore, the wide alkalinity range was due to the presence of bicarbonate ions. After this short initial period, the alkalinity trend fluctuated to reach a stable value of approximately 22 mg/L $CaCO_3$, which is approximately equal to that of the

influent water alkalinity. In the initial days of filtration, the pH of the M1, M2, and M3 permeates showed a minimum value of 6.3–6.6, which is based on the alkalinity graph. The pH data were consistent with those obtained for alkalinity. The pH stabilized at a value equivalent to that of the influent (7.5) once the initial neutralization period of the membranes was complete.

3.6. Biofilm characterization results

To discriminate the biofouling layer using OCT, an image without a biofilm layer (virgin membrane) was compared with another image with the biofilm layer on the membrane surface (Figure S5). Digital camera photos of the synthesized membranes after 65 days of filtration (the last day of the experiment) are shown in Figure 7. The OCT images of membranes M1, M2, and M3 after 15, 30, and 45 days of filtration are shown in Figure S6. The images taken on the last filtration day (day 65) are shown in Figure 8. According to the images taken after 15 days of filtration (Figure S6, a, b, c), a distinct heterogeneous and outspread layer of biofilm was observed. After day 30, a denser, more compact, and aggregated biofouling layer was observed as shown in Figure S6d-h, especially for the M2 and M3 membranes (for M1 membranes, there was still an outspread biofilm structure on day 30). At the end of the experiment, based on the images taken on day 65 (Figure 8 a, b, c), the most compact and dense biofilm structure was observed on the membrane surface.

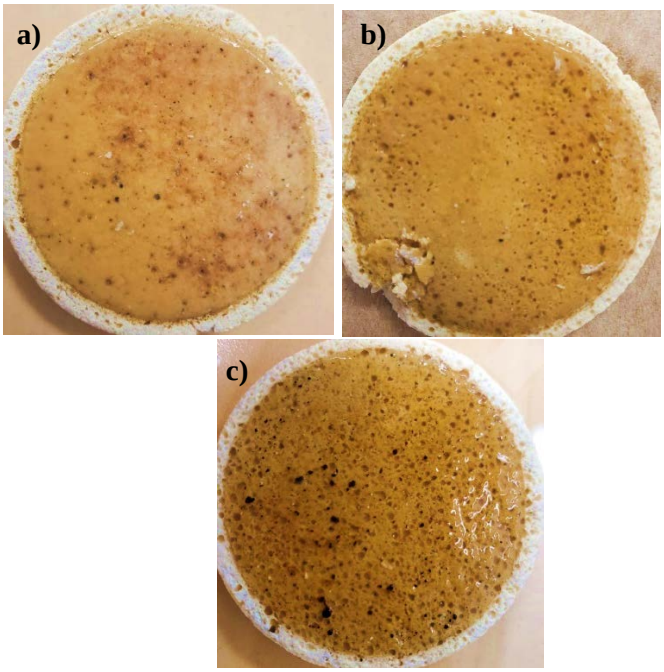

Figure 7. Digital photographs of a) M1 (kaolin only), b) M2 (75 Wt% kaolin + 25 Wt% alumina), and c) M3 (50 Wt% kaolin + 50 Wt% alumina) membranes on day 65

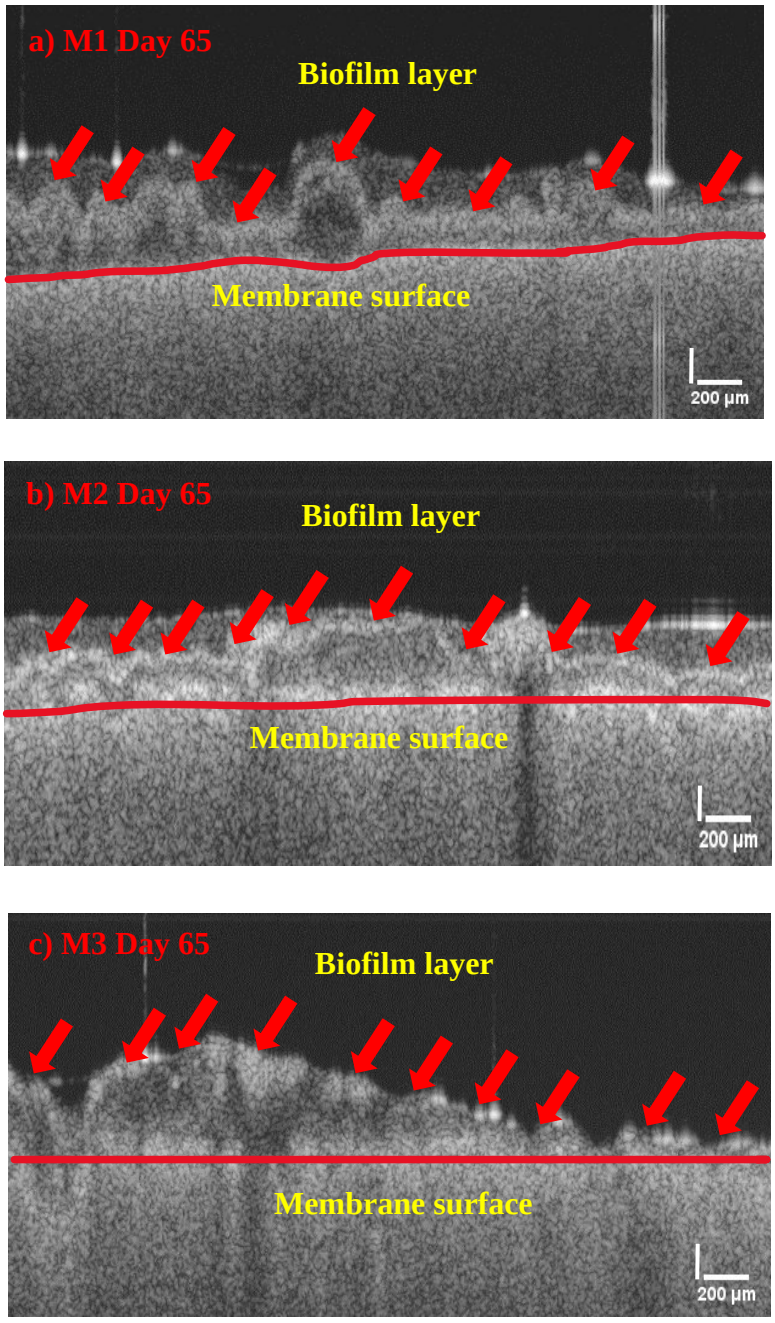

Figure 8. OCT images of a) M1 (kaolin only), b) M2 (75 Wt% kaolin + 25 Wt% alumina), and c) M3 (50 Wt% kaolin + 50 Wt% alumina) membrane surfaces on day 65

To study the effect of the membrane structure on biofilm formation, the absolute and relative roughness and mean thickness of the biofilm layer were determined (Table 7), using the OCT images acquired at the end of the experiment (day 65). For the membrane without alumina in its structure (M1), the mean thickness and absolute roughness were 371 and 104 μm, respectively. For the membrane with 25% wt alumina (M2), the absolute roughness and mean thickness were calculated to be 224 and 70 μm, respectively. For M3, the mean biofilm layer thickness was 315 μm, and the absolute roughness was 173 μm. The relative roughness values for M1, M2, and M3 were calculated to be 0.28, 0.31, and 0.55, respectively.

Table 6. Mean biofilm thickness and relative and absolute roughness of the biofilm based on the OCT images acquired on day 65

Parameter	M1	M2	M3
$\bar{Z}$ (μm)	371	224	315
R_a(μm)	104	70	173
$\overline{R_a}$	0.28	0.31	0.55

To quantify the total active microorganisms present in the biofouling layer, the ATP concentration was measured in the biofilm layer (Figure 9). According to the graph, the mATP/m membrane ratio for M3 had the highest value of 6.3×10^{-8}, which is approximately three times more than that for M2 (2×10^{-8}) and ten times higher than that for M1.

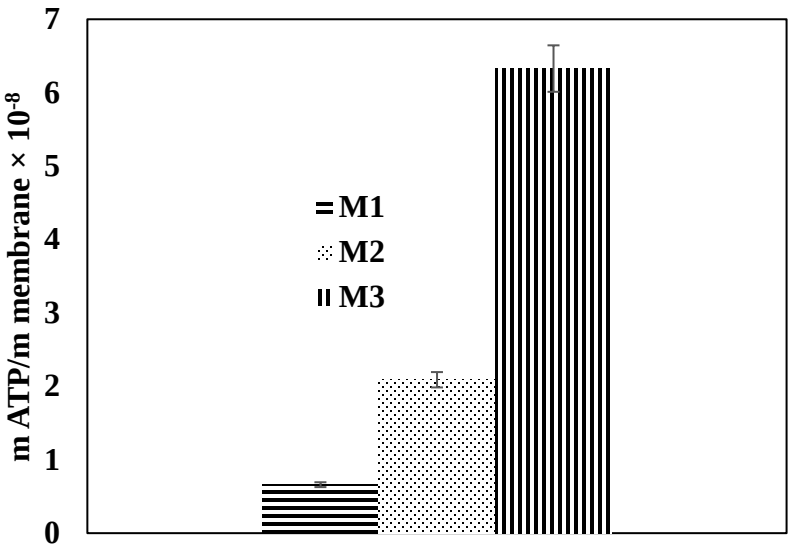

Figure 9. Ratio of $m_{ATP}/ m_{membrane}$ for the three synthesized membranes: M1 (kaolin only), M2 (75 Wt% kaolin + 25 Wt% alumina), and M3 (50 Wt% kaolin + 50 Wt% alumina)

4. Discussion

4.1. OCT observations confirm the flux decline modeling results

Based on the images acquired on day 15 of filtration, before reaching a stable flux (Figure S5, a, b, c), a distinct heterogeneous and outspread layer of biofilm was observed. As explained in the flux modeling section (section 3.4), before reaching a stable flux (approximately before day 24 for the synthesized membranes), the fouling mechanism is controlled by pore blocking mechanisms (standard, intermediate, and complete), not the cake layer, which were confirmed by the OCT observations, showing a scattered and sporadic biofilm structure. During the initial period, the steep flux decline might be related to the decrease in the effective membrane pore volume (i.e., pore blocking mechanisms) (Akanbi, Hernandez et al. 2018). After flux stabilization for the synthesized membranes, it was possible to observe a more compact and aggregated cake layer based on Figure S6d, e, and f. After blocking the inside volume of the pores, it was expected that the contaminants accumulate on the membrane surface; consequently, a more compact biofouling/cake layer was observed. The transition of the pore blocking models to cake layer formation makes it possible to achieve a stable flux (Figure S6 g, h, i), as reported elsewhere in the literature (Akanbi, Hernandez et al. 2018).

According to the images taken on day 65 (Figure 8 a, b, c), the most compact cake layer structure was observed on the membrane surface. In fact, in long-term and continuous filtration, the interaction between contaminant particles in the influent water on the membrane surface and the force exerted by the TMP were the factors compressing the biofouling layer formed on the membrane surface. Therefore, a relatively level biofilm layer with a dense internal structure is observed during long-term filtration (Derlon, Peter-Varbanets et al. 2012, Derlon, Koch et al. 2013, Shi, Liu et al. 2020). Based on these observations, it is more realistic to discuss the roughness and thickness of the biofilm at the end of the filtration time, where the most compact biofouling structure was observed.

Consistent with the values listed in Table 6, the relative biofilm roughness for M1, M2, and M3 showed an ascending trend for increasing alumina concentration in the membrane structure. The relative roughness coefficient indicated the homogeneity and uniformity of the biofilm. Increasing the alumina concentration in the membrane structure increased the heterogenicity of the biofilm structure formed on their surfaces. Therefore, in the case of M3, at the end of filtration (day 65), the relative roughness showed the highest value, indicating the formation of the most heterogeneous biofilm structure.

4.2. Increase in biomass concentration in the biofilm is due to increased membrane adsorption capacity

Owing to the presence of higher alumina content in the M3 structure, which improves the adsorption conditions of the particles and contaminants, more biomass can accumulate on the membrane surface, which eventually enhances the microbial activity in the biofilm (Figure 9). Furthermore, increased adsorption of organic matter on the alumina-enriched membrane leads to an increase in the nutrient concentration on the membrane surface consumed by the microorganisms present in the biofilm, which finally increases the number of microbial species in M3 (Vieira and Melo 1995, Shao, Feng et al. 2017).

4.3 Effect of membrane structure on permeate flux and fouling resistance

In this study, a four-stage flux flow was observed for all synthesized membranes, regardless of their structure and alumina concentration. The four stages consisted of: i) a steep flux decline section before reaching the stabilized flux, ii) a constant flux section, iii) a slight flux increase, and iv) a constant flux regime. Therefore, no effect of the alumina concentration and membrane structure was observed on the general flux decline diagram behavior. However, the effect of increasing the alumina concentration in the membrane structure (M1 = 0 Wt% alumina, M2 = 25 Wt% alumina, and M3 = 50 Wt%) on the flux was clearly observed in the initial days of filtration, before reaching a stable flux. In this stage, the greater the alumina content in the membrane structure was, the higher the flux and the steeper the flux decline curve were. However, after reaching a stable flux, the alumina concentration had a negligible effect, as the flux at the end of the filtration time was roughly the same for the synthesized membranes (2.5 LMH for M1 and M2 and 3 LMH for M3). These results suggest that increasing alumina content in the membrane

structure can increase the permeate flux prior to the section of reaching a stable flux. However, stable flux is roughly independent of the membrane structure, as reported for polymeric membranes (Frechen, Exler et al. 2011, Lee, Lee et al. 2019). Nevertheless, in the literature both flux rise or drop can be found following modifications of surface properties or structure. The pre-deposition of zeolite on the surface of UF membranes showed an increased membrane fouling in both short-term and long-term GDM, however a higher stable flux was observed for GDM using zeolite and powdered activated carbon adsorbents combined with the membrane (Ding, Song et al. 2021). Furthermore, altering membrane characteristics by depositing a layer of granular activated carbon on the membrane surface resulted in an improved organic removal, decreased stable flux and increased hydraulically reversible resistance (Ding, Wang et al. 2018). The researchers in another study (Jiang, Zhao et al. 2019) modified the matrix of Polyvinylidene Fluoride membranes using synthetic tailored amphiphilic multi-arms polymer poly(propylene glycol)-silane-poly(ethylene glycol). The results revealed an increased porosity and hydrophilicity of the membranes compared to membranes without modification. The water flux of modified membranes in GDM process increased from 4.6 LMH to 12.1 LMH compared to control membranes (without modification).

Likewise, the general trend of fouling resistance for all the membranes followed three stages: i) a steep increase roughly to the flux stabilization point, ii) a decrease, and iii) eventually reaching a stable value. In the case of the synthesized membranes, regardless of their alumina content, the values of fouling resistance were approximately equal for most of the filtration time, indicating that increasing the alumina concentration in the membrane structure does not markedly affect the fouling resistance. However, it has been reported that using adsorption of a granular activated carbon as a thin layer on the polymeric membrane surface can increase fouling resistance (Ding, Wang et al. 2018a).

4.4 Effect of membrane structure and bio-clogging on permeate quality

Permeate quality can be affected by two main factors: adsorption (by alumina in the membrane structure) and biodegradation/biosorption (by the biofilm/cake layer). Regarding permeate turbidity, during the initial filtration days before reaching a flux stabilization time, a poor cake layer effect occurred, as revealed by the OCT images and flux modeling results. Therefore, adsorption played a key role in turbidity removal, as M1 (0 Wt% alumina), M2 (25 Wt% alumina) and M3 (50 Wt%).

The highest and lowest turbidity values are shown in Figure 6a. After reaching a stable flux and a compact biofilm structure, the turbidity removal values increased. This can be related to the formation of a biofilm/cake layer on the membrane surface, which acts as a bio-filter medium, decreasing the turbidity content (Akanbi, Hernandez et al. 2018).

Likewise, the higher DOC and UV_{254} absorbance removal in M2 and M3 compared with that in M1, at the beginning of filtration, can be attributed to their higher adsorption capacity. Moreover, the QCM confirmed the higher affinity of the alumina-based membranes (M2 and M3) toward NOM (higher NOM deposition on the Al_2O_3 sensors). DOC and UV_{254} rejection after reaching a stable flux can be attributed to the formation of a cake layer on the membrane surface that operates as an extra filter medium (Discart, Bilad et al. 2014). The DOC removal of M3 was slightly lower than M2, despite the increased alumina content of M3 compared to M2. Generally, a higher NOM removal is expected by the membrane with the enhanced adsorption capacity (M3), however increasing alumina concentration in the membrane structure increased the porosity and membrane pore size, which decreases the organic rejection of the membrane because of a smaller contact time in the membrane. The mechanism of increasing the permeate quality after reaching a stable flux is mainly due to the biological activity of the biofilm layer on the membrane surface (Pronk, Ding et al. 2019). During the GDCM process, the porous membrane is responsible for rejecting larger contaminants in the influent water, such as colloidal matter (turbidity removal), and the formed biofilm is expected to improve the removal of dissolved organic matter, because the biofilm can act as a secondary membrane or biodegradation agent for organic matter (Chawla, Zwijnenburg et al. 2017, Pronk, Ding et al. 2019).

5 Conclusions

In this study, three types of ceramic microfiltration membranes based on kaolin clay and different alumina contents were synthesized, and their performance for gravity-driven filtration of river water was investigated. The membrane characteristics were studied using different methods (SEM, XRD, mean pore size and porosity calculations, and contact angle). The effects of alumina content and biofouling on steady-state flux and permeate quality (turbidity, DOC, UV_{254}, pH, and alkalinity) were investigated. The following conclusions were drawn:

- For the synthesized membranes (M1, M2, and M3), the stable flux was roughly the same at the end of the filtration (2.5–3.0 LMH), indicating that the stable flux state is independent of the alumina content.
- The synthesized membranes showed significant UV_{254}, alkalinity, and DOC removal during the initial filtration days, as well as turbidity removal after flux stabilization.
- The modeling flux decline revealed that the dominant membrane fouling mechanism before reaching a stable flux corresponds to pore blocking. After reaching a stable flux, fouling was dominated by cake layer formation.
- The OCT imaging observations showed a distinct heterogeneous biofilm layer before a stable flux was achieved, followed by a dense and irregular cake layer formation, confirming the transformation of the mechanism from pore blocking model to cake layer formation model.
- Increasing the alumina content in the membrane structure leads to enhanced carbon adsorption, resulting in the deposition of more nutrients in the biofilm layer, which enhances the biological activity, as measured through the ATP method.

For future objectives, smaller pore size membranes (0.1–0.2 µm) should be tested to reach a permeate turbidity below 0.1 NTU. Moreover, according to the flux and fouling resistance results, the physical and chemical cleaning stages and pretreatment such as resins which are operating in biological mode could be added to increase the sustainability of the process.

6. Acknowledgements

The authors would like to express their gratitude to the Polytechnique Montreal technicians and research professionals, Gabriel St-Jean, Julie Philibert, Mélanie Bolduc, Tetiana Elyart, Jacinthe Mailly, and Yves Fontaine for their help in preparing the gravity-driven membrane filtration setup and raw water and for their technical support during this project. The authors would like to thank Nathalie Tufenkji for sharing the QCM equipment used in this study. This project was funded by the Canada Research Chair for Decentralized and Small-Scale Water Treatment (file number 950-232871).

7. References

Akanbi, M., L. Hernandez, M. Mobarok, J. Veinot and N. J. E. S. N. Tufenkji (2018). "QCM-D and NanoTweezer measurements to characterize the effect of soil cellulase on the deposition of PEG-coated TiO 2 nanoparticles in model subsurface environments." Environmental Science: Nano **5**(9): 2172-2183.

Akhondi, E., B. Wu, S. Sun, B. Marxer, W. Lim, J. Gu, L. Liu, M. Burkhardt, D. McDougald and W. J. w. r. Pronk (2015). "Gravity-driven membrane filtration as pretreatment for seawater reverse osmosis: linking biofouling layer morphology with flux stabilization." Water research **70**: 158-173.

Arzani, M., H. R. Mahdavi, O. Bakhtiari and T. J. C. I. Mohammadi (2016). "Preparation of mullite ceramic microfilter membranes using Response surface methodology based on central composite design." Ceramics International **42**(7): 8155-8164.

Bakke, R., R. Kommedal and S. Kalvenes (2001). "Quantification of biofilm accumulation by an optical approach." Journal of Microbiological Methods **44**(1): 13-26.

Chawla, C., A. Zwijnenburg, A. J. B. Kemperman and K. Nijmeijer (2017). "Fouling in gravity driven Point-of-Use drinking water treatment systems." Chemical Engineering Journal **319**: 89-97.

Derlon, N., N. Koch, B. Eugster, T. Posch, J. Pernthaler, W. Pronk and E. J. W. r. Morgenroth (2013). "Activity of metazoa governs biofilm structure formation and enhances permeate flux during Gravity-Driven Membrane (GDM) filtration." Water research **47**(6): 2085-2095.

Derlon, N., J. Mimoso, T. Klein, S. Koetzsch and E. J. W. r. Morgenroth (2014). "Presence of biofilms on ultrafiltration membrane surfaces increases the quality of permeate produced during ultra-low pressure gravity-driven membrane filtration." Water research **60**: 164-173.

Derlon, N., M. Peter-Varbanets, A. Scheidegger, W. Pronk and E. J. W. r. Morgenroth (2012). "Predation influences the structure of biofilm developed on ultrafiltration membranes." Water research **46**(10): 3323-3333.

Ding, A., H. Liang, G. Li, I. Szivak, J. Traber and W. Pronk (2017). "A low energy gravity-driven membrane bioreactor system for grey water treatment: Permeability and removal performance of organics." Journal of Membrane Science **542**: 408-417.

Ding, A., J. Wang, D. Lin, R. Zeng, S. Yu, Z. Gan, N. Ren, G. Li and H. Liang (2018a). "Effects of GAC layer on the performance of gravity-driven membrane filtration (GDM) system for rainwater recycling." Chemosphere **191**: 253-261.

Discart, V., M. Bilad, L. Marbelia and I. J. B. t. Vankelecom (2014). "Impact of changes in broth composition on Chlorella vulgaris cultivation in a membrane photobioreactor (MPBR) with permeate recycle." Bioresource technology **152**: 321-328.

Du, X., Y. Liu, R. Ma, M. Xiao, W. Yang, X. Han, Y. Luo, Z. Wang and H. J. C. Liang (2021). "Gravity-driven ceramic membrane (GDCM) filtration treating manganese-contaminated surface water: Effects of ozone (O3)-aided pre-coating and membrane pore size." Chemosphere **279**: 130603.

Frechen, F. B., H. Exler, J. Romaker and W. Schier (2011). "Long-term behaviour of a gravity-driven dead end membrane filtration unit for potable water supply in cases of disasters." Water Supply **11**(1): 39-44.

Fujimoto, J. G. and W. Drexler (2015). Optical Coherence Tomography: Technology and Applications, Springer.

Hermia, J. (1982). "Constant pressure blocking filtration laws: application to power-law non-Newtonian fluids."

Hernández, M. F., M. A. Violini, M. F. Serra, M. S. Conconi, G. Suarez and N. M. Rendtorff (2020). "Boric acid (H3BO3) as flux agent of clay-based ceramics, B2O3 effect in clay thermal behavior and resultant ceramics properties." Journal of Thermal Analysis and Calorimetry **139**(3): 1717-1729.

Hubadillah, S. K., M. H. D. Othman, T. Matsuura, A. F. Ismail, M. A. Rahman, Z. Harun, J. Jaafar and M. Nomura (2018). "Fabrications and applications of low cost ceramic membrane from kaolin: A comprehensive review." Ceramics International **44**(5): 4538-4560.

Issaoui, M. and L. Limousy (2019). "Low-cost ceramic membranes: Synthesis, classifications, and applications." Comptes Rendus Chimie **22**(2): 175-187.
Klein, T., D. Zihlmann, N. Derlon, C. Isaacson, I. Szivak, D. G. Weissbrodt and W. J. W. r. Pronk (2016). "Biological control of biofilms on membranes by metazoans." Water research **88**: 20-29.
Lapointe, M., J. M. Farner, L. M. Hernandez, N. J. E. s. Tufenkji and technology (2020). "Understanding and improving microplastic removal during water treatment: impact of coagulation and flocculation." Environmental science & technology **54**(14): 8719-8727.
Lee, D., Y. Lee, S. S. Choi, S.-H. Lee, K.-W. Kim, Y. J. E. S. Lee and P. Research (2019). "Effect of membrane property and feed water organic matter quality on long-term performance of the gravity-driven membrane filtration process." Environmental Science and Pollution Research **26**(2): 1152-1162.
Maltais-Tariant, R., C. Boudoux and N. Uribe-Patarroyo (2020). "Real-time co-localized OCT surveillance of laser therapy using motion corrected speckle decorrelation." Biomedical Optics Express **11**(6): 2925-2950.
Oka, P. A., N. Khadem and P. R. Bérubé (2017). "Operation of passive membrane systems for drinking water treatment." Water Research **115**: 287-296.
Peter-Varbanets, M., F. Hammes, M. Vital and W. Pronk (2010). "Stabilization of flux during dead-end ultra-low pressure ultrafiltration." Water Research **44**(12): 3607-3616.
Pronk, W., A. Ding, E. Morgenroth, N. Derlon, P. Desmond, M. Burkhardt, B. Wu and A. G. J. W. r. Fane (2019). "Gravity-driven membrane filtration for water and wastewater treatment: a review." Water research **149**: 553-565.
Rashad, M., G. Logesh, U. Sabu and M. Balasubramanian (2021). "A novel monolithic mullite microfiltration membrane for oil-in-water emulsion separation." Journal of Membrane Science **620**: 118857.
Rasouli, Y., M. Abbasi and S. A. Hashemifard (2017). "Investigation of in-line coagulation-MF hybrid process for oily wastewater treatment by using novel ceramic membranes." Journal of Cleaner Production **161**: 545-559.
Rasouli, Y., M. Abbasi and S. A. J. J. o. A. C. S. Hashemifard (2019). "Fabrication, characterization, fouling behavior and performance study of ceramic microfiltration membranes for oily wastewater treatment." Journal of Asian Ceramic Societies **7**(4): 476-495.
Sauerbrey, G. (1959). "Use of quartz crystal units for weighing thin films and microweighing." *Magzine for Physics* **1959**, *155*, 206-222. **155**: 206-222.
Shao, S., Y. Feng, H. Yu, J. Li, G. Li and H. J. W. r. Liang (2017). "Presence of an adsorbent cake layer improves the performance of gravity-driven membrane (GDM) filtration system." Water research **108**: 240-249.
Shi, D., Y. Liu, W. Fu, J. Li, Z. Fang and S. J. W. R. Shao (2020). "A combination of membrane relaxation and shear stress significantly improve the flux of gravity-driven membrane system." Water research **175**: 115694.
Truttmann, L., Y. Su, S. Lee, M. Burkhardt, S. Brynjólfsson, T. H. Chong and B. J. J. o. W. P. E. Wu (2020). "Gravity-driven membrane (GDM) filtration of algae-polluted surface water." Journal of Water Process Engineering **36**: 101257.
Vieira, M. J. and L. F. Melo (1995). "Effect of clay particles on the behaviour of biofilms formed by pseudomonas fluorescens." Water Science and Technology **32**(8): 45-52.
Wu, B., S. R. Suwarno, H. S. Tan, L. H. Kim, F. Hochstrasser, T. H. Chong, M. Burkhardt, W. Pronk and A. G. Fane (2017). "Gravity-driven microfiltration pretreatment for reverse osmosis (RO) seawater desalination: Microbial community characterization and RO performance." Desalination **418**: 1-8.
Zhang, X., W.-Z. Lang, H.-P. Xu, X. Yan and Y.-J. J. R. A. Guo (2015). "The effects of hydroxyapatite nano whiskers and its synergism with polyvinylpyrrolidone on poly (vinylidene fluoride) hollow fiber ultrafiltration membranes." RSC Advances **5**(28): 21532-21543.